applied sciences

MDPI

Article

Characterization of Reduced Graphene Oxide (rGO)-Loaded SnO_2 Nanocomposite and Applications in C_2H_2 Gas Detection

Lingfeng Jin [1,2,*], Weigen Chen [1,2], He Zhang [1,2], Gongwei Xiao [1,2], Chutian Yu [1,2] and Qu Zhou [1,3]

1 State Key Laboratory of Power Transmission Equipment & System Security and New Technology, Chongqing University, Chongqing 400044, China; weigench@cqu.edu.cn (W.C.); sophy305410@163.com (H.Z.); xgw2012@126.com (G.X.); 20151113076t@cqu.edu.cn (C.Y.); zhouqu@swu.edu.cn (Q.Z.)
2 School of Electrical Engineering, Chongqing University, Chongqing 400044, China
3 College of Engineering and Technology, Southwest University, Chongqing 400715, China
* Correspondence: cqujlf@cqu.edu.cn; Tel.: +86-23-6511-1795 (ext. 8223)

Academic Editor: Volodymyr Khranovskyy
Received: 31 October 2016; Accepted: 17 December 2016; Published: 23 December 2016

Abstract: Acetylene (C_2H_2) gas sensors were developed by synthesizing a reduced graphene oxide (rGO)-loaded SnO_2 hybrid nanocomposite via a facile two-step hydrothermal method. Morphological characterizations showed the formation of well-dispersed SnO_2 nanoparticles loaded on the rGO sheets with excellent transparency and obvious fold boundary. Structural analysis revealed good agreement with the standard crystalline phases of SnO_2 and rGO. Gas sensing characteristics of the synthesized materials were carried out in a temperature range of 100–300 °C with various concentrations of C_2H_2 gas. At 180 °C, the SnO_2–rGO hybrid showed preferable detection of C_2H_2 with high sensor response (12.4 toward 50 ppm), fast response-recovery time (54 s and 23 s), limit of detection (LOD) of 1.3 ppm and good linearity, with good selectivity and long-term stability. Furthermore, the possible gas sensing mechanism of the SnO_2–rGO nanocomposites for C_2H_2 gas were summarized and discussed in detail. Our work indicates that the addition of rGO would be effective in enhancing the sensing properties of metal oxide-based gas sensors for C_2H_2 and may make a contribution to the development of an excellent ppm-level gas sensor for on-line monitoring of dissolved C_2H_2 gas in transformer oil.

Keywords: SnO_2 nanoparticles; reduced graphene oxide; nanocomposite; dissolved gases in transformer oil; acetylene gas sensor; gas sensing mechanism

1. Introduction

Condition monitoring and fault diagnosis is crucial in ensuring the long-term safe and stable operation of power transformers. Latent faults in the power transformer in early stages can be found by monitoring the operation state of the insulation system, which mainly consists of oil and paper [1]. The occurrence of incipient thermal or discharge faults cause the C-H and C-C bond cleavage of oil-paper insulation system, leading to the formation of various dissolved gases, such as H_2, CH_4, C_2H_6, C_2H_4 and C_2H_2 [2]. These gases turn into insulated defects, which reduce the insulation strength of the oil-paper insulation system and develop into permanent faults. The composition and content of these dissolved gases must be detected in order to identify types and severity, as well as to accurately assess the insulation status of power transformer [3–5]. In addition, Acetylene (C_2H_2) is a colorless combustible hydrocarbon. It is the simplest alkyne, with a distinctive odor. It is widely used as a fuel and in many other industrial applications. For example, it is an important raw material for organic

synthesis such as in 2-chloro-1,3-butadiene; in lighting; in welding and metal cutting; and in dry-cell batteries, etc. However, it is extremely unstable in its pure form and it is easy to incur fire or explosive accidents when it is liquefied, compressed, heated or mixed with air. Thus, the safety monitoring of C_2H_2 is vital during its production and handling. Use of gas sensors is one of the most widely and effectively used methods to detect the composition and content of C_2H_2 gas [6].

Metal oxides (MOs) that change their electrical conductance while exposed to ambient gas can be utilized as gas sensing materials [7]. Many MOs are applicable to detect the reducing and oxidizing gases, for instance, the conductance of CuO, NiO, In_2O_3, WO_3, TiO_2, Fe_2O_3, etc. show different response to gases. However, ZnO and SnO_2 are the main gas sensing materials for commercial applications and experimental research [8]. Pure SnO_2 is sensitive to all the dissolved gases, but it still has some shortcomings, such as high heating temperature, unsatisfied response and poor selectivity [9].Research on how to efficiently improve gas sensing properties is focused on surface modification [10], doping [11] and morphology or size control [12,13]. Recently, graphene has attracted much attention because of its two-dimensional nanostructure with extremely high specific area and electron mobility. The graphene sensor is expected to exhibit excellent gas sensing performance [14]. However, pure graphene is composed of periodic, closely-packed carbon atoms with a benzene ring structure, which is unfavorable for the adsorption of gas molecules. In this regard, the graphene derivative, which is decorated with oxygen functional groups to increase the adsorption site for gas molecules, was named reduced graphene oxide (rGO) [15]. In particular, many groups have reported the gas sensing properties of rGO-based materials, loaded with MOs nanoparticles, with respect to various gases. The NiO–rGO nanocomposite exhibited high response, good repeatability and acceptable selectivity toward CH_4 gas detection [16]. ZnO–rGO exhibited significantly higher responses than pure ZnO with respect to various gases, including O_2, SO_2, NO_2, CO, C_6H_6, and C_2H_5OH [17]. The MO–rGO (SnO_2, Fe_2O_3 and NiO) composite porous films exhibited much better sensing performances than those of the corresponding pure oxide films in detecting C_2H_5OH gas [18]. TiO_2–rGO shows good sensitivity and excellent selectivity to different concentrations of NH_3 from 5 ppm to 50 ppm at room temperature [19]. Latif and Dickert summarized the recent progress and gas sensing applications in graphene hybrid materials, including fabrication method of graphene-based sensors, nanostructures of hybrid materials, gas sensing mechanisms and future perspectives [20]. Nevertheless, there is few reports about the gas sensing properties of SnO_2 nanoparticle–reduced graphene oxide (SnO_2–rGO) nanocomposites for C_2H_2 gas detection at a ppm level.

Herein, we investigated the gas sensing properties (including optimum operating temperature, response to concentration, dynamic sensing transient, response and recovery time, selectivity and long-term stability) of SnO_2–rGO nanocomposites with respect to C_2H_2 gas detection. The SnO_2–rGO nanomaterials were synthesized via a simple two-step hydrothermal method and characterized by X-ray diffraction (XRD), transmission electron microscopy (TEM), energy dispersive spectroscopy (EDS), Raman spectra, X-ray photoelectron spectroscopy (XPS) and thermogravimetric analyses (TGA). Meanwhile, planar sensors were fabricated to examine the gas sensing performance with respect to C_2H_2 gas. The results indicate that the SnO_2–rGO can efficiently detect the C_2H_2 gas under a low operating temperature, showing better sensing performances than those of rGO alone. Finally, the possible gas sensing mechanisms of the SnO_2-rGO with respect to C_2H_2 detection have been discussed.

2. Experimental Method

2.1. Materials

The commercially available high-purity graphene oxide (GO) was purchased from XFNANO Materials Technology Co., Ltd. (Nanjing, China). Sodium stannate hydrate ($Na_2SnO_3 \cdot 3H_2O$), citric acid hydrate ($C_6H_8O_7 \cdot H_2O$) and sodium hydroxide (NaOH) were purchased from Chuandong Chemical Reagent Co., Ltd. (Chongqing, China). All chemicals in our work were of analytical reagent grade and used as-received, without any further purification.

2.1.1. SnO_2 Nanoparticle Synthesis

SnO_2 nanoparticles were synthesized by the following hydrothermal method [21]. First, 2.5 mmol of $Na_2SnO_3 \cdot 3H_2O$ and 1.0 mmol of $C_6H_8O_7 \cdot H_2O$ were dissolved in the mixture of 20 mL deionized water (DIW) and 20 mL anhydrous ethanol (EtOH), and the solution was vigorously stirred for 10 min. Subsequently, 15 mmol of NaOH was added dropwise into the above solution and stirred vigorously for 30 min. Then, the precursor solution was transferred to a 50 mL Teflon-lined autoclave which was heated at 180 °C for 14 h. Afterwards, the product was collected after centrifuging and washing for several times. Finally, the product was calcined at 400 °C for 2 h.

2.1.2. SnO_2–rGO Nanocomposite Preparation

SnO_2–rGO was prepared by compositing as-prepared SnO_2 nanoparticles and GO under the hydrothermal treatment and the detailed preparation process was presented as follows. The same amount (5 mg) of as-prepared SnO_2 nanoparticles and GO were added into 30 mL of DIW with stirring and ultrasonic dispersion for 30 min to achieve uniform dispersion. Then, the dispersion solution was transferred to 50 mL Teflon autoclave (180 °C, 12 h). The products were centrifuged and calcined at 200 °C for 2 h to obtain the SnO_2-rGO nanocomposite. For comparison, the rGO was prepared by the similar method without addition of SnO_2.

2.1.3. Characterization

The microstructure and morphology of as-prepared samples were characterized. X-ray diffraction (XRD) patterns were recorded on a Bruker D8 Advance (Bruker, Karlsruhe, Germany) using Cu Kα radiation at 40 kV and 40 mA. Raman spectra were determined using a HORIBA Jobin Yvon LabRam (HORIBA Jobin Yvon, Paris, France) equipped with a 532 nm wavelength laser and full-range grating. Thermogravimetric analyses (TGA) were carried out with a NETZSCH STA 449F3 (Netzsch, Selb, Germany) unit at a heating rate of 5 °C/min under a nitrogen atmosphere. Scanning electron microscopy (SEM) images were observed by a FEI Nova Nano Field Emission SEM (FEI, Hillsboro, OR, USA) operated at 20 kV. Transmission electron microscopy (TEM) and energy dispersive spectroscopy (EDS) images were performed by an FEI Tecnai G^2 F20 S-TWIN (FEI, Hillsboro, OR, USA) operated at 200 kV. The Thermo ESCALAB 250Xi spectrometer (Thermo Fisher Scientific, Waltham, MA, USA) was used to recorded the X-ray photoelectron spectroscopy (XPS) images.

2.2. Fabrication of Planar Gas Sensor

Aiming at testing the gas sensing of as-synthesized gas sensing nanomaterials, a planar resistivity-type sensor device was fabricated. The sensor is mainly made up of three layers: sensing materials, Ag–Pd electrodes and Al_2O_3 substrate. For the planar sensor depicted in Figure 1, Ag–Pd electrodes were interdigitally etched on Al_2O_3 with ≈300-nm-thick foil, 0.2-mm electrode width and spacing by screen-printing. The Ag–Pd pastes (9:1 by weight ratio) used in our experiment have been used for chemical sensors in many cases [22,23]. These substrates can work in atmospheres under 300 °C with stable electric and chemical properties, which are based on the interactions of Pd-doping in Ag pastes. The required quantity of nanocomposites was evenly dispersed in the mixture of DI water and ethanol ratio of 1:1, then the paste was dispersed coated onto the interdigital area of Ag–Pd electrodes to form uniform, dense and smoothly deposited thick films by screen-printing technique [24,25]. Finally, after drying overnight, aging occurred at 120 °C for 120 h to ensure surface resistance value remained stable. For this reason, the stability and repeatability of planar sensor was enhanced.

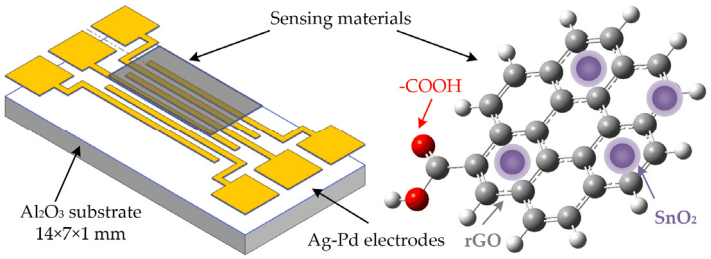

Figure 1. Schematic diagram of the SnO_2–reduced graphene oxide (rGO) nanocomposite planar gas sensor.

2.3. Gas Sensing Measurements

The gas sensing properties of the fabricated planar gas sensor for C_2H_2 were tested by our gas sensing analysis measurement system, which is made up of an automatic gas distribution equipment and the CGS-1TP intelligent gas sensing analysis system (Elite Technology Co., Ltd., Beijing, China), is shown in Figure 2. This measurement system is convenient for controlling and obtaining the experimental parameters (operating temperature, resistance characteristic, ambient condition, etc.).

The procedure of testing is described below. First, the fabricated planar gas sensor was fixed in the center of heating stage by two adjustable probes, which were used to collect the electrical signals of the sensing materials. Then, the operating temperature of sensor was set and air was delivered into a sealed chamber at a constant flow rate. When the resistance of the sensor remained stable, the C_2H_2 gas was injected into the chamber. After the response was achieved, the gas sensor was exposed to air again. The concentration of C_2H_2 gas was controlled by the mass flow controllers (MFCs) with the following equation:

$$\mathrm{Gas}_{\mathrm{concentration}}(\mathrm{ppm}) = \frac{\text{Flow rate}_{C_2H_2}}{\text{Flow rate}_{\mathrm{air}} + \text{Flow rate}_{C_2H_2}} \quad (1)$$

The sensor was measured at temperatures ranging between 100 °C and 300 °C for various concentrations of C_2H_2. The response of a sensor is calculated as $S = R_a/R_g$, where R_a and R_g are the resistances of the sensor in the air and C_2H_2 gas at certain concentrations, respectively. Response time and recovery time of the sensor were defined as the time required to reach 90% of the total resistance change [26]. The whole experiment process conducted at the same environment temperature and relative humidity (25 °C, 35%).

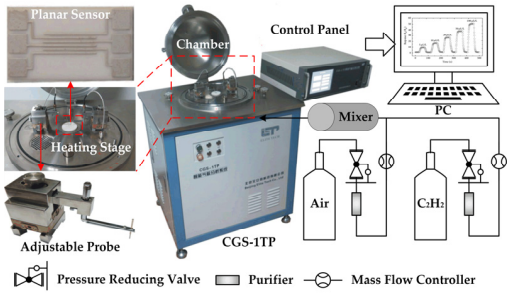

Figure 2. Real image and schematic diagram of the gas sensing analysis measurement system.

3. Results and Discussion

3.1. Structural Characterization

The samples must be characterized before the measurement of gas sensing performance to identify the microstructure and morphology. The XRD patterns of rGO, SnO_2 and SnO_2–rGO are presented

in Figure 3a. It is seen that a broad diffraction peak centered at $2\theta = 24.5°$ with interlayer distance of 3.78 Å of rGO was observed, which is close to the typical (002) diffraction peak of graphite at $2\theta = 26.6°$. The peak of GO which might appear in the range of 2θ (10°–12°) was not observed, which further indicates that the GO had been almost completely reduced to rGO. Meanwhile, several strong peaks appeared at 2θ of 26.6°, 33.7°, 37.8° and 51.6°, in agreement with the (110), (101), (200) and (211) planes of rutile SnO_2 (JCPDS 77-0452). The main diffraction peaks of SnO_2–rGO were similar with those of SnO_2 and the characteristic peak of rGO is invisible as seen in Figure 3a, probably owing to the fact that the rGO is wrapped by SnO_2 nanocrystals through the hydrothermal treatment, or that the weak peak of rGO is swamped by the presence of the strong peak around 26.6° at (110) plane of the SnO_2 nanocrystals [27]. Figure 3b shows the Raman spectrum results of SnO_2–rGO, which can be used to prove the existence of rGO in the SnO_2–rGO nanocomposite. Two representative peaks were observed around at 1355 cm^{-1} and 1586 cm^{-1}, corresponding with disorder-induced (D) band and tangential (G) band of rGO. Due to the ultrasonic exfoliation and hydrothermal treatment, the GO was reduced and more defects were introduced which enhance the performance of gas adsorption, leading to the D and G band of rGO having some minor peak shifts to 1360 cm^{-1} and 1608 cm^{-1} of GO. Moreover, the three typical peaks located at round 472 cm^{-1}, 641 cm^{-1} and 781 cm^{-1} can be matched with the E_g, A_g and B_{2g} vibration modes of rutile SnO_2 [28]. All these mentioned characteristic peaks appeared in the Raman spectrum of SnO_2–rGO. It was confirmed that the as-synthesized SnO_2–rGO nanocomposite was made up of rGO and SnO_2. The characteristics of combustion of SnO_2–rGO were investigated using thermogravimetric analysis (TGA) and the results are as shown in Figure 3c. The first 2.199% mass loss (approximately 100 °C) was due to water solvent molecules absorbed into the reduced GO bulk material. The following 5.096% decrease (400 °C) represents elimination of the remaining functional groups; further decomposition takes place up to 800 °C. Experimental settings were as follows: temperature scanning rate: 5 °C/min; temperature range 30–800 °C, and purging inert gas: N_2. SnO_2–rGO has good thermal stability in the range of temperatures (100–300 °C).

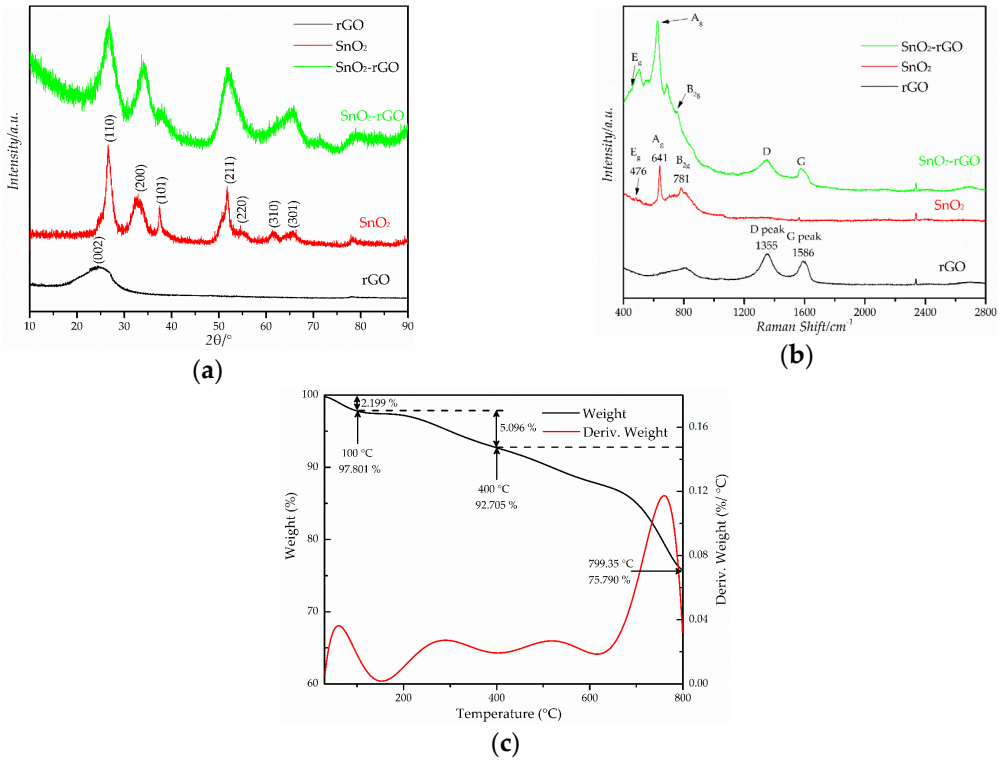

Figure 3. (**a**) X-ray diffraction (XRD) patterns; (**b**) Raman spectra of rGO, SnO_2 and SnO_2–rGO samples; and (**c**) thermogravimetric analyses (TGA) results of SnO_2–rGO nanocomposites.

Figure 4a depicts the TEM and high-resolution TEM (HRTEM) micrographs of rGO. The quality of rGO is good because of its excellent transparency and obvious fold boundary. In Figure 4b, the SnO_2 nanoparticles with irregular grain size up to 10 nm in diameter were successfully synthesized. From the TEM image of SnO_2–rGO in Figure 4c,d, it can be seen that the SnO_2 nanoparticles were uniformly loaded on the rGO nanosheet surface. Meanwhile, the neighboring fringe spacing of the nanoparticle, dispersed on the surface of rGO, was 0.34 nm. This can be attributed to (110) plane of SnO_2 nanocrystals, indicating that the SnO_2–rGO nanocomposites were prepared. Figure 4e shows the selected area electron diffraction (SAED) pattern of SnO_2–rGO; all diffraction rings on this SAED pattern were exactly assigned to the reflections (110), (101), (211), (112) of the rutile SnO_2 phase and (002) of rGO, which agree well with the XRD pattern of SnO_2–rGO in Figure 3a. The energy dispersive spectroscopy (EDS) spectrum of SnO_2–rGO indicated that the Sn element is found in the constituent elements of SnO_2–rGO (C, O and Sn) and the content of the Sn element was calculated as 15.737 wt %, further verifying that SnO_2 was loaded on the surface of rGO.

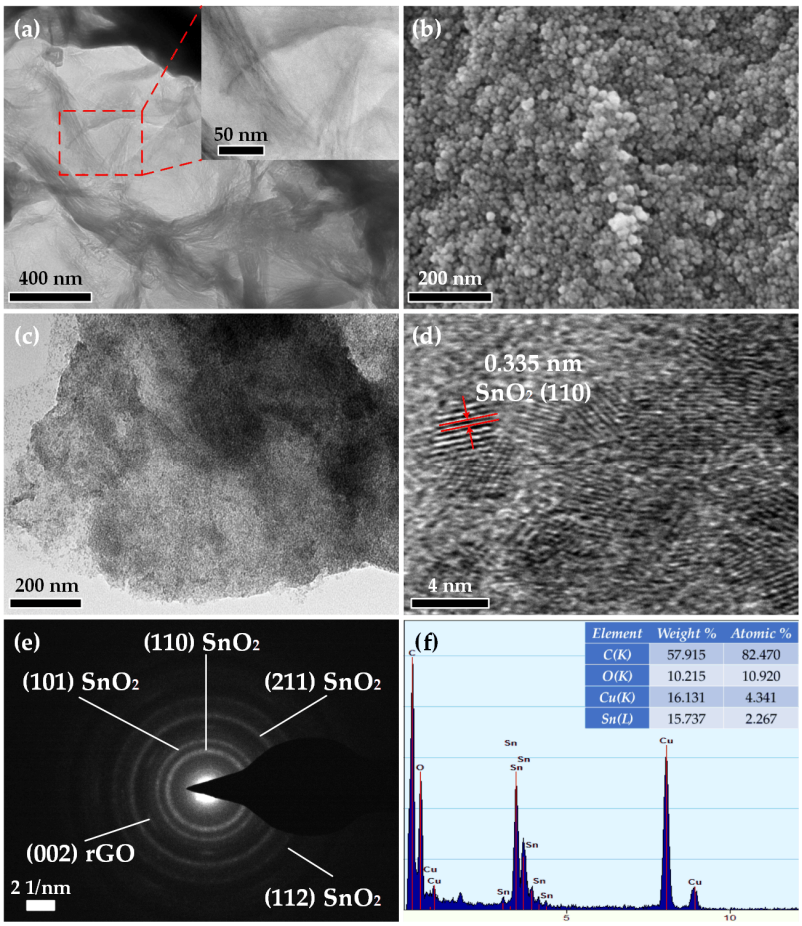

Figure 4. (**a**) Transmission electron microscopy (TEM) micrograph of rGO (the inset shows the HRTEM (high-resolution TEM) image of rGO); (**b**) Scanning electron microscopy (SEM) image of pristine SnO_2 nanoparticles; (**c**) TEM image; and (**d**) HRTEM of SnO_2–rGO nanocomposites; (**e**) selected area electron diffraction (SAED) pattern; and (**f**) the EDS (energy dispersive spectroscopy) spectrum of SnO_2–rGO.

To further investigate the composition and chemical state of the element, X-ray photoelectron spectroscopy (XPS) spectra of the SnO_2–rGO nanocomposite were carried out and are shown in Figure 5. As depicted in Figure 5a, the peaks of C 1s, O 1s, Sn 4d, Sn 3d and Sn 3p can be observed in survey spectrum. The two peaks with binding energies of 487.5 eV and 496.0 eV corresponded to Sn $3d_{5/2}$ and Sn $3d_{3/2}$ respectively, which indicated the existence of Sn^{2+}. Figure 5c shows the C 1s

spectrum and binding energy of C-C, C-O; C=O and O-C=O are assigned at 284.7 eV, 285.6 eV, 286.8 eV and 288.9 eV, respectively [29]. Figure 5d displays the O 1s spectrum, which has been separated into three peaks at 530.4 eV, 531.5 eV and 533.7 eV. The peak centered at 530.4 eV was attributed to oxidized metal ions (O_L) in the lattice of Sn–O. The binding energy at 531.5 eV is ascribed to oxygen vacancies (O_V) in the surface of SnO_2–rGO. The high binding energy peak located at 533.7 eV originated from the oxygen atoms (O_S) chemisorbed on the surface of synthesized materials [30]. Based on above results, it is concluded that the as-synthesized nanocomposites are composed of SnO_2 and rGO.

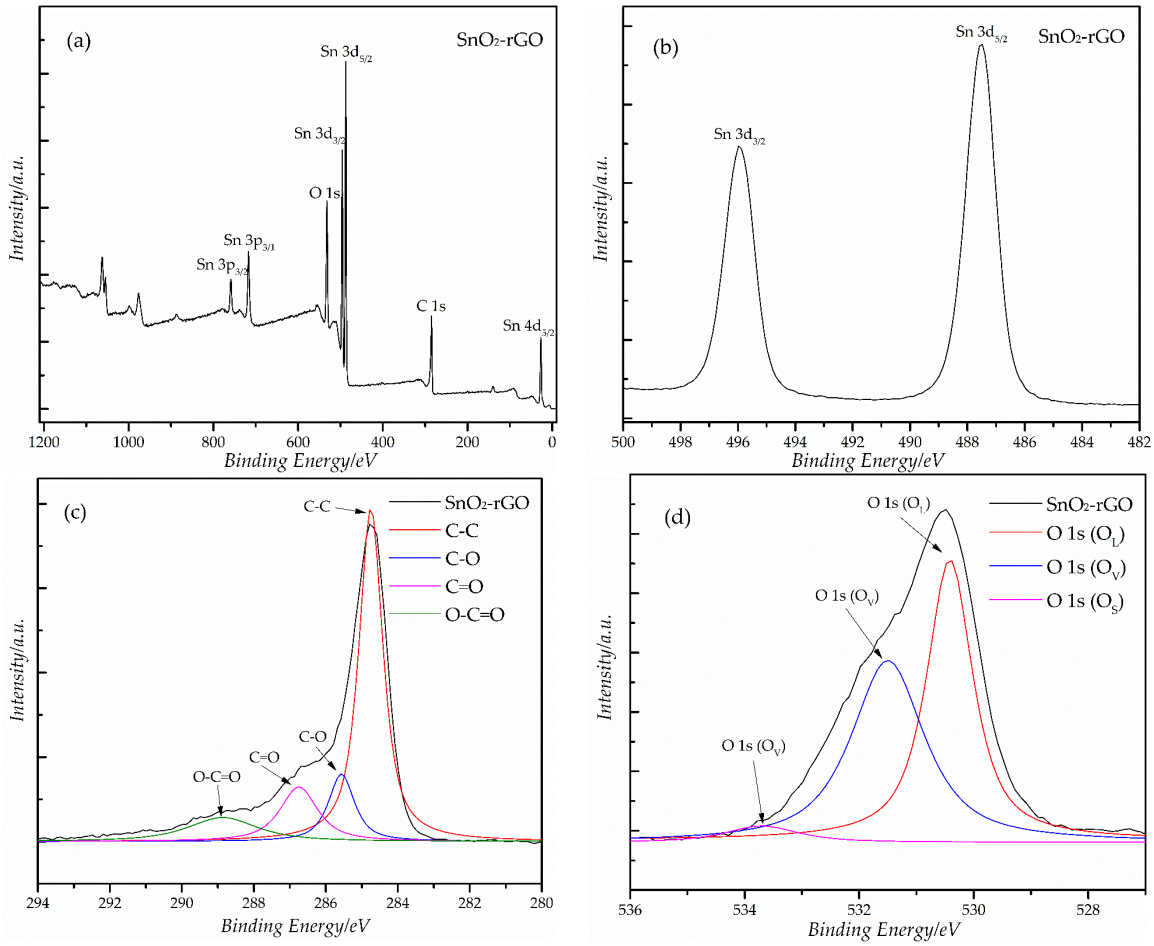

Figure 5. XPS (X-ray photoelectron spectroscopy) spectra of (**a**) survey of SnO_2–rGO; (**b**) Sn 3d region of SnO_2–rGO; (**c**) C 1s region of SnO_2–rGO; and (**d**) O 1s region of SnO_2–rGO.

3.2. C_2H_2 Gas Sensing Properties

C_2H_2 gas is one of the main fault characteristic gases dissolved in power transformer oil, which can indicate the transformer discharge faults effectively. Thus, we carried out the gas sensing properties of the fabricated gas sensors for C_2H_2 gas. Figure 6a shows the resistance curve (resistance of the sensor in the air versus temperature) of rGO, SnO_2 and SnO_2–rGO gas sensors. Then the operating temperatures of rGO, SnO_2 and SnO_2–rGO gas sensors were investigated at a temperature range of 100 °C to 300 °C, with an interval of 20 °C. Figure 6b shows the relationship between response and temperature for those gas sensors to 50 ppm C_2H_2 gas. It is obvious that the responses of rGO–SnO_2 first ascended and then descended with the temperature increasing, while those of rGO and SnO_2 increased slowly in the temperature range of measurement. Although the reduced graphene oxide gas sensor shows a good response to gases at room temperature [31], the SnO_2 gas sensor usually works at high temperatures (about 360 °C) [32]. This behavior might be attributed to the potential

barrier formed by the chemisorbed oxygen ions ($O_n^-{}_{(ads)}$) on the SnO_2 surface, which prevents the C_2H_2 molecules from reacting at low temperature. The SnO_2 gas sensor at low temperature possibly underwent a small chemical activation (the adsorption–desorption kinetics of test gas on the sensing materials), and showed a small response. At high temperatures, due to the enhanced chemical activation, the adsorbed gas molecules may escape before their reaction, leading to a response drop. Due the presence of SnO_2 in the SnO_2–rGO nanocomposite, the optimum operating temperature is between that of rGO and SnO_2. The operating temperature when the response of SnO_2–rGO reached the maximum value about 12.4 was 180 °C, which is called the optimum operating temperature and proved that the introduction of rGO was beneficial to reducing the optimum operating temperatures for the SnO_2-based gas sensor.

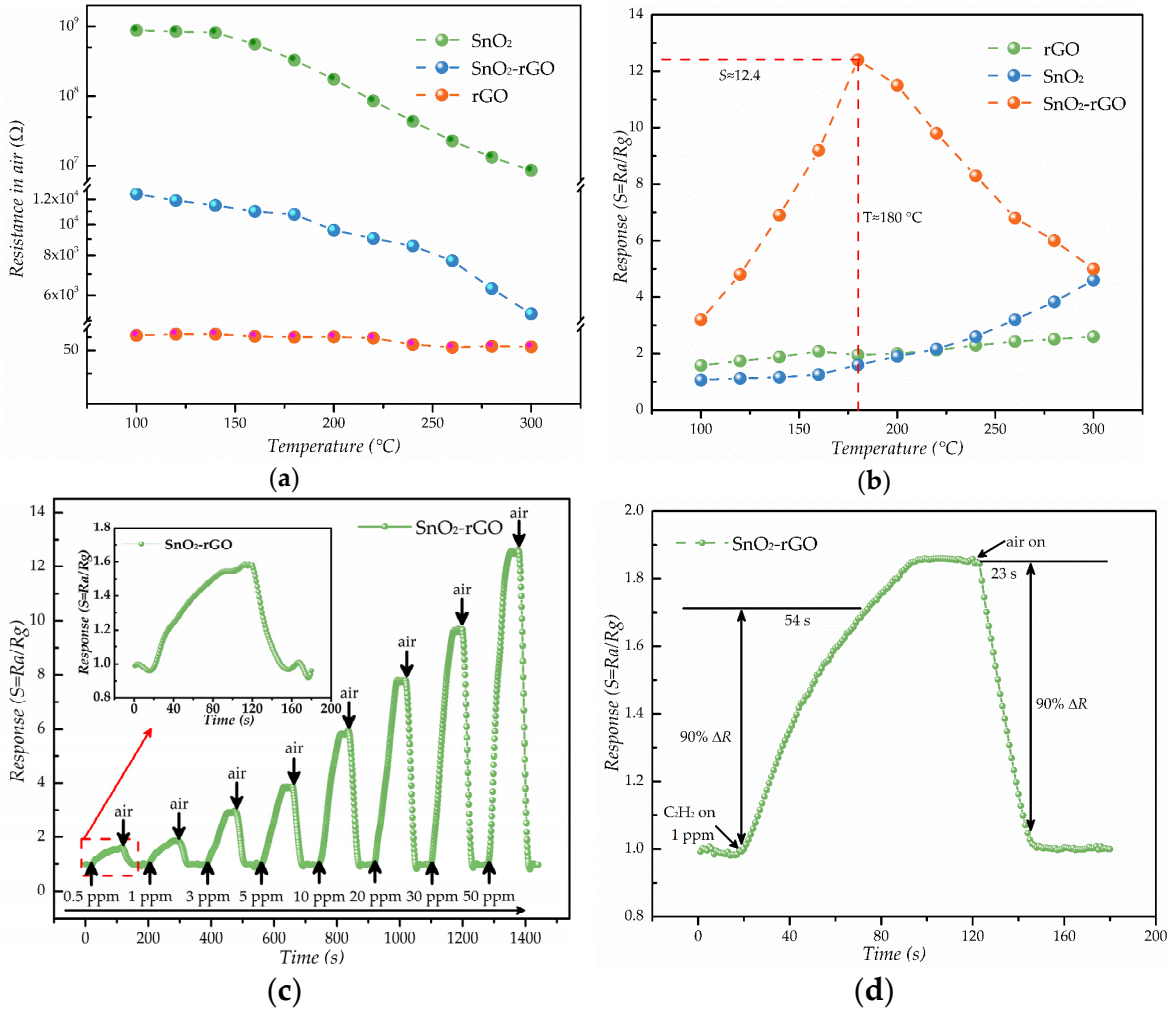

Figure 6. Results of C_2H_2 gas sensing properties: (**a**) Resistance of the SnO_2, rGO and SnO_2–rGO gas sensors at different operating temperatures; (**b**) Response of the rGO, SnO_2 and SnO_2–rGO gas sensors to 50 ppm C_2H_2 gas at different operating temperatures; (**c**) Response under different gas concentrations from 0.5 ppm to 50 ppm for C_2H_2 of SnO_2–rGO at 180 °C; (**d**) Dynamic sensing transient of SnO_2–rGO sensor to 1 ppm C_2H_2 gas.

Figure 6c shows the response-recovery curve of SnO_2-rGO to different concentrations of C_2H_2 gas from 0.5 ppm to 50 ppm at its optimum operating temperature (180 °C). When SnO_2–rGO gas sensor was exposed to the C_2H_2 gas, its response clearly increased. In contrast, the response of SnO_2–rGO gas sensor was decreased backed to the initial state after air was delivered into the chamber. To further study the response-recovery performance, the dynamic sensing transient of SnO_2–rGO sensor to 1 ppm

C_2H_2 gas was shown in Figure 6d. By definition, the response and recovery times of SnO_2–rGO were estimated to be around 54 s and 23 s, respectively.

The response curve of SnO_2–rGO gas sensor to various concentrations (from 0.5 ppm to 500 ppm) of C_2H_2 gas at optimum operating temperatures of 180 °C was plotted in Figure 7a. The response of sensor increased steeply from 0.5 ppm to 10 ppm and then increased slowly from 10 ppm to 500 ppm. Sensitivity is one of the most important parameters, which measures the variation of the response as a function of the variation of the concentration (c). The figure of the sensitivity as shown in Figure 7a can be calculated as the derivative of the response curve of SnO_2–rGO. Moreover, Figure 7b shows that response versus concentration maintained good linearity when the gas concentration was below 10 ppm, with R^2 = 0.994, and the equation for the response y and concentration x can be depicted as:

$$y = 0.447x + 1.421 \quad (2)$$

In this case, we defined that the limit of detection is the lowest concentration when the response reached 2. Thus, it can be calculated that when sensing response (y) goes to 2 the concentration (x) goes to 1.3 ppm.

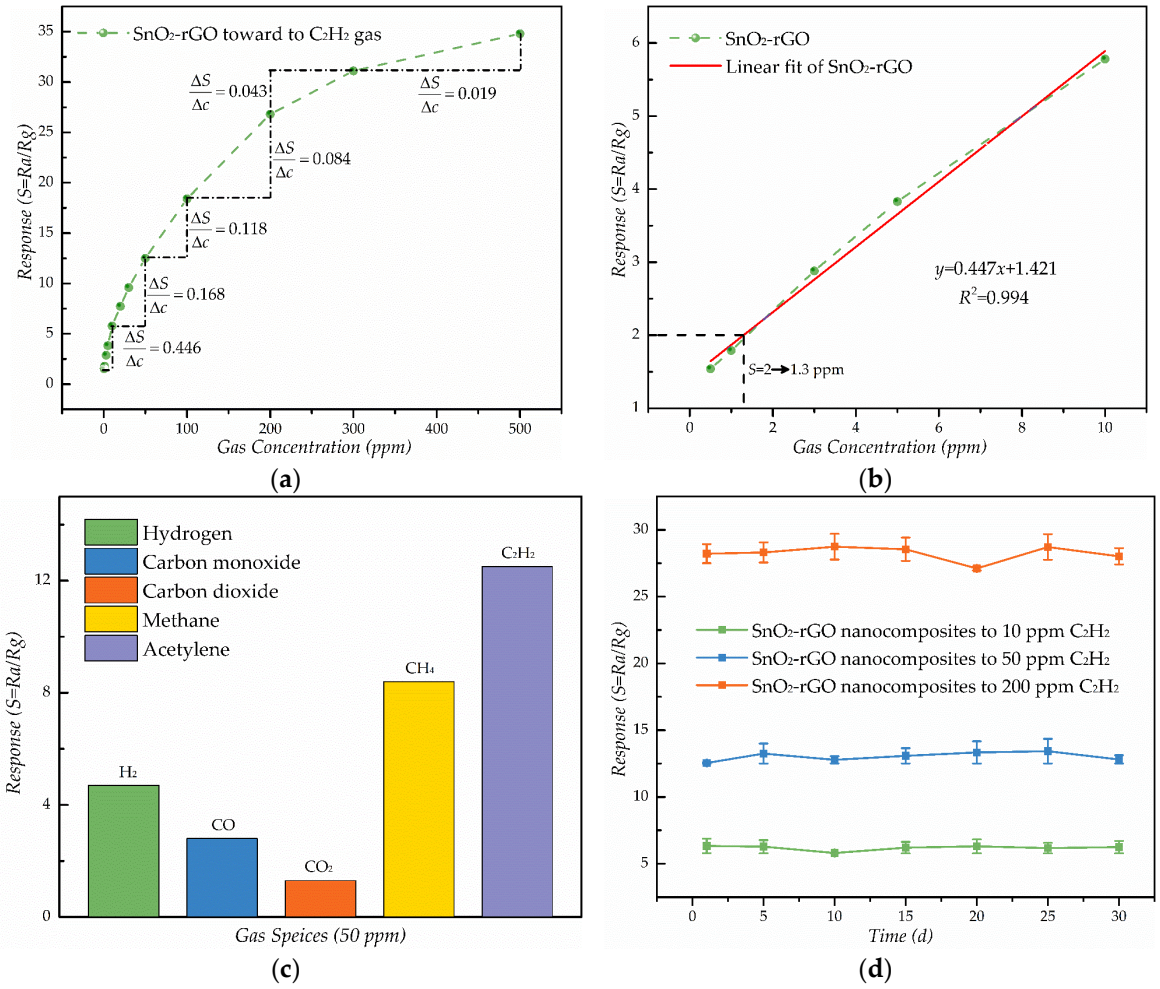

Figure 7. (**a**) Corresponding response variations of the SnO_2–rGO sensor as a function of C_2H_2 gas concentrations at 180 °C; (**b**) The limit of detection and the linear relationship between response and concentration; (**c**) Response of SnO_2–rGO gas sensors to 50 ppm different gases (hydrogen, carbon monoxide, carbon dioxide, methane and acetylene) and (**d**) The stability of SnO_2–rGO sensor with respect to 10, 50 and 200 ppm C_2H_2, respectively.

Generally, a chemical sensor may be sensitive not only to its intended chemical for measurement, but also to a number of chemicals that can equally be present in the environment, so selectivity is another important property of gas sensors. The figure of the selectivity can be calculated using Equation (13) presented in [33]. The response of SnO_2–rGO gas sensors to 50 ppm different gases (hydrogen, carbon monoxide, carbon dioxide, methane and acetylene) at 180 °C are described in Figure 7c. The highest response is observed for C_2H_2 sensing performance, which is almost 2.7, 4.5, 9.6 and 1.5 times higher than for H_2, CO, CO_2 and CH_4, respectively. All those results reveal that the SnO_2–rGO sensor can be used for C_2H_2 detection. Better response to C_2H_2 might be attributed to higher reactivity and smaller bond energy of H-C≡C-H (490 kJ/mol) compared with other test gases. Although the bond energy of CH_4 (431 kJ/mol) and H_2 (436 kJ/mol) is close to C_2H_2, interaction strength between the sensing layer and target gas is an effective factor on the sensor response [34]. In the case of the SnO_2–rGO gas sensor, H_2 and CO may decompose easily at about 200 °C, where the exothermic reactions become impulsive, hence showing higher response [35]. The fabricated sensor did not show a remarkable response toward CO_2 due to insufficient interaction strength between sensing layer and exposed gas [36]. Moreover, based on the molecular frontier orbital theory, we calculated the highest occupied molecular (HOMO) and lowest unoccupied molecular (LUMO) values of hydrocarbon gases and conducted response testing of SnO_2. The results showed that the ability of losing electron weakens in the following order: C_2H_4, C_2H_2, C_2H_6 and CH_4, which is in strong agreement with our experimental data [32]. Generally, sensor selectivity is a complicated problems associated with the intricate film nanostructure and complicated sensing mechanisms. Sensor selectivity may need further investigation with respect to critical applications [37]. Furthermore, the stability of SnO_2–rGO sensor upon exposure to 10 ppm, 50 ppm and 200 ppm C_2H_2 gas was investigated. The measurements lasted for 30 days and responses were tested every 5 days. As shown in Figure 7d, the responses to 10 ppm, 50 ppm and 100 ppm C_2H_2 gas were kept at an almost constant level. These observed results demonstrate that the proposed sensor has good long-term stability. Lastly, the comparison of the C_2H_2 gas sensing properties of the SnO_2/rGO gas sensor with previously reported results in C_2H_2 gas sensors using other nanomaterials are shown in Table 1.

Table 1. Comparison of previously reported and our work on C_2H_2 gas sensors.

Ref.	Material	Temperature (°C)	Measuring Range (ppm)	Response ($S = R_a/R_g$)	$\tau_{Response}$ (s)	$\tau_{Recovery}$ (s)
[38]	Pure SnO_2	300	200–10,000	6.3 (10,000 ppm)	34	>10 min
[39]	Sm_2O_3/SnO_2	180	1–5000	63.8 (1000 ppm)	3	17
[40]	Pt/ZnO	300	50–10,000	43 (1000 ppm)	6	65
[41]	ZnO/rGO [1]	250	30–1000	18.2 (100 ppm)	100	28
Our	SnO_2–rGO	180	0.5–500	12.4 (50 ppm)	54	23

[1] rGO: reduced graphene oxide.

3.3. Gas Sensing Mechanism

According to our experimental results, SnO_2–rGO nanocomposites have excellent performance with respect to detection of C_2H_2, which shows potential for application. The possible sensing mechanism is discussed as follows. Commonly, the sensing mechanism of MO gas sensors is explained by the adsorption–desorption model, the resistance changes of the MOs through the interaction between adsorbed oxygen ions (O^{2-}, O^- or O_2^-) and target gas molecules. As we know, rGO nanosheets prepared by chemical or thermal treatment will show a *p*-type semiconductor characteristic [42]. Thus, the heterojunctions (*n*-*n* or *n*-*p*) can be formed when rGO is composited with MOs. This will affect the gas sensing performance by impacting on the resistances change of the nanocomposites. In order to explain the gas sensing mechanism in SnO_2–rGO nanocomposites as thoroughly as possible, several possible mechanisms will be considered, as follows.

Firstly, the nanostructure of as-synthesized SnO_2 grains are composed of nanoparticles, as shown in Figure 8b. The adsorption–desorption model and boundary barrier model are described in Figure 8a. As the SnO_2 works as a *n*-type semiconductor characteristic, when the SnO_2 grain is exposed to the air, the O_2 molecules in air will adsorbed on the surface of the SnO_2 grain to form the adsorbed oxygen ions (O^{2-}, O^- or O_2^-). As the electrons on the surface of SnO_2 are captured by O_2 molecules, a wide electron depletion layer (DL) is formed. When the SnO_2 which contains adsorbed oxygen ions comes into contact with reducing gases, the trapped electrons will release back to the surface of SnO_2 and the width of the DL will be reduced. For example, the possible interaction of C_2H_2 has been proposed in the reference [41] as follows:

$$O_2 + 2e^- \leftrightarrow 2O^-(ads) \quad (3)$$

$$C_2H_2 + O^-(ads) \rightarrow CO_2 + H_2O + e^- \quad (4)$$

Meanwhile, the electron transfer between different SnO_2 nanoparticles is an important factor for gas sensing behavior. If the electron in the nanoparticle is to transfer to another, the boundary barrier which is formed by space charge must be overcome. The contact resistance in the interface will affect the resistance of the gas sensor. When the SnO_2 is in the air, the electron on the surface of SnO_2 will be trapped and the boundary is raised. In contrast, in the reducing gases the electron is released back to the surface and the barrier is lowered. The increase or decrease of the width of the DL and boundary barrier according to the interaction between adsorbed oxygen ions make an important contribution to the sensing performance of SnO_2.

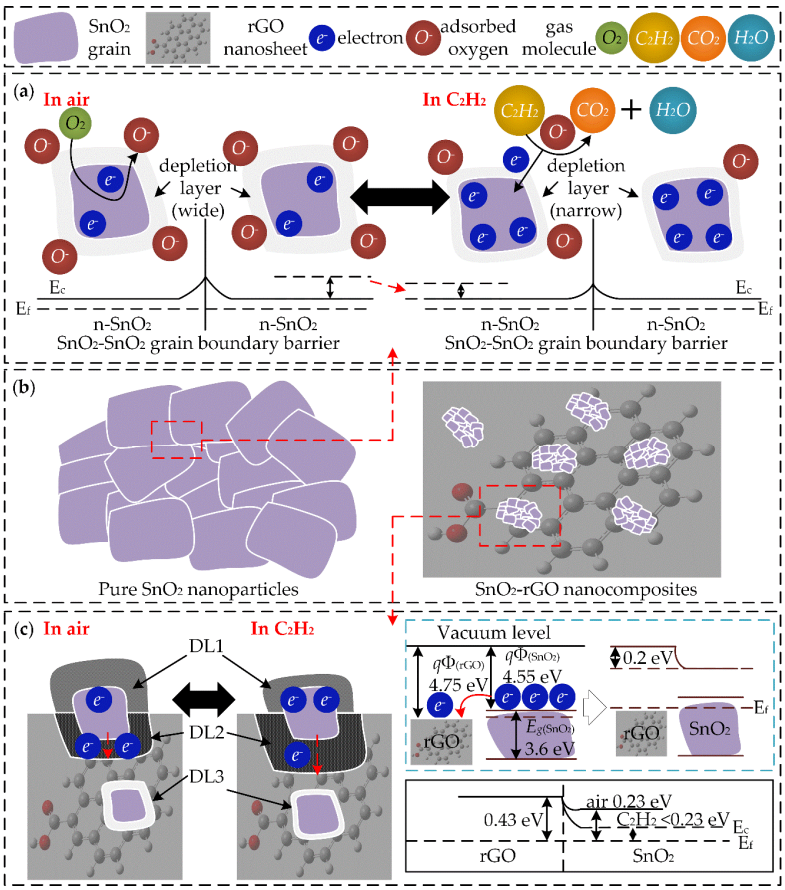

Figure 8. (**a**) Schematic illustration of sensing mechanism of pure SnO_2 nanoparticles; (**b**) structure of SnO_2 nanoparticles and SnO_2–rGO nanocomposites; and (**c**) schematic illustration of sensing mechanism of SnO_2–rGO nanocomposites.

Secondly, for SnO_2–rGO nanocomposites possessing *n*-type character, electrons acted as electron carriers. The structure of SnO_2–rGO is shown in Figure 8b and the mechanism is investigated in Figure 8c. When it is exposed to air, three types of electron DL may be formed, as shown in Figure 8c. DL1 is the first electron depletion layer, which is formed on the surface of SnO_2 nanoparticles owing to the adsorbed oxygen ions [43]; DL2 is the second electron depletion layer, which is formed by the electrons and transfers from the surface of SnO_2 to the rGO during the formation of *p-n* heterojunctions; and DL3 is the third electron depletion layer. It appears in the area where SnO_2 is embed in rGO nanosheets and forms the *p-n* heterojunctions [18]. All these electron depletion layers will prevent the migration of electron, leading to the high-resistance state of the nanocomposites. When the reducing gas is introduced, the width of these three types DLs will undergo different changes. The trapped electrons in the DL1 will be released back to the SnO_2, decreasing the width of the DL1; generally, that of DL2 is supposed to be decreased because the reducing gas molecules may be adsorbed on the surface of rGO and donate the electrons to it. However, the work functions of SnO_2 and rGO are 4.55 eV and 4.75 eV, respectively. Because the work function of SnO_2 is smaller than that of rGO, the electrons in SnO_2 will transfer to rGO to equate the Fermi level and form a barrier (0.2 eV), as shown in Figure 8c. While the reducing gas is introduced, the value of (E_C-E_F) in SnO_2 will decrease the barrier for electron transfer from SnO_2 to rGO. As a result, the number of electrons in SnO_2 will be sufficient, leading to a smaller resistance of SnO_2 and a broadened width of DL2. Through the relative resistance change of SnO_2 is much larger than that of rGO, the width of DL3 in *p-n* heterojunctions is reduced. The specific nanostructure of SnO_2-rGO nanocomposites which could cause the different types of electron depletion layers has made great contribution to the change of resistance.

Thirdly, the formation of *p-n* heterojunctions between SnO_2 and rGO can help to enhance the gas sensing properties, and includes many other factors. As the rGO is obtained by chemical or thermal treatment of graphene oxide, there may be many oxygen functional groups on the surface of rGO, such as hydroxyl (-OH) and carboxyl (-COOH) which will provide more adsorption sites for the formation of adsorbed oxygen ions and target gas molecules [44,45]. Besides, the introduction of rGO can effectively prevent the aggregation of SnO_2 nanoparticles, because there are many overlaps among the SnO_2 nanoparticles that must be generated, reducing the exposed active surface [18]. Due to these factors, the resistance variation shows a larger change when compared to individual SnO_2 or rGO.

According to the proposed possible mechanisms, we conclude that the SnO_2-rGO gas sensing mechanism combines with the effect of the adsorbed oxygen ions and grain boundary barrier of SnO_2, the structural characteristics of rGO and the formation of local *p-n* heterojunctions between SnO_2 and rGO. All these sources can be considered as the resistance modulation of the SnO_2–rGO nanocomposites. We suggest that the combination of two sensing mechanisms, being related to rGO-SnO_2 *p-n* heterojunctions and structural characteristics of rGO, is responsible for the enhancement of the gas sensing properties of rGO-loaded SnO_2. Thus, we can safely conclude that this hybrid sensing mechanism, which combines the effects of high specific surface area and local *p-n* heterojunctions, is primarily responsible for the enhancement of the sensitivity. In comparison, the adsorbed oxygen ions (O^{2-}, O^- or $O_2{}^-$) and grain boundary barrier of SnO_2 will make contributions to the enhancement of the gas sensing properties for most of metal oxide semiconductor-based gas sensor. However, the rGO-SnO_2 *p-n* heterojunctions (change of electron depletion layer), oxygen functional groups and high specific surface area (greater number of adsorption sites) are special characteristics for rGO–SnO_2 hybrid materials due to the due to the presence of rGO. Further investigations to study the exact sensing mechanism are needed.

4. Conclusions

This paper demonstrated a high performance C_2H_2 gas sensor based on a SnO_2–rGO nanocomposite, which was synthesized via a facile two-step hydrothermal method. The as-prepared SnO_2-rGO nanocomposites were characterized by XRD, Raman, TEM, EDS and XPS. The planar gas sensor was fabricated to investigate the gas sensing properties of C_2H_2 gas. The gas sensing properties

of the as-fabricated planar gas sensor to C_2H_2 were tested using exposure to various concentrations of C_2H_2 gas at the optimum operating temperature (180 °C). The C_2H_2 gas sensor exhibited a good dynamic response (0.5–50 ppm), low limit of detection (1.3 ppm), high response (S = 12.4–50 ppm), fast response–recovery time (54 s, 23 s), good selectivity, long-term stability and maintained good linearity from 0.5 ppm to 10 ppm. Furthermore, the possible gas sensing mechanisms of the SnO_2–rGO nanocomposites were summarized and discussed. Our work may contribute to the development of a ppm-level gas sensor for on-line monitoring of dissolved C_2H_2 gas in transformer oil.

Acknowledgments: This work was supported by the National 111 Project of the Ministry of Education of China (No. B08036) and the Funds for the Excellent Achievements Transformation of Chongqing Universities (No. KJZH17101).

Author Contributions: Lingfeng Jin and Weigen Chen conceived and designed the experiments; Lingfeng Jin and He Zhang performed the experiments; Gongwei Xiao and Chutian Yu analyzed the data; Lingfeng Jin wrote the paper. Lingfeng Jin, Weigen Chen and Qu Zhou reviewed and revised the manuscript. All authors read and approved the manuscript.

Conflicts of Interest: The authors declare no conflict of interest.

References

1. Saha, T.K. Review of modern diagnostic techniques for assessing insulation condition in aged transformers. *IEEE Trans. Dielectr. Electr. Insul.* **2003**, *10*, 903–917. [CrossRef]
2. Arshad, M.; Islam, S.M. Significance of cellulose power transformer condition assessment. *IEEE Trans. Dielectr. Electr. Insul.* **2011**, *18*, 1591–1598. [CrossRef]
3. Duval, M. A review of faults detectable by gas-in-oil analysis in transformers. *IEEE Electr. Insul. Mag.* **2002**, *18*, 8–17. [CrossRef]
4. Wang, M.; Vandermaar, A.J.; Srivastava, K.D. Review of condition assessment of power transformers in service. *IEEE Electr. Insul. Mag.* **2002**, *18*, 12–25. [CrossRef]
5. Bengtsson, C. Status and trends in transformer monitoring. *IEEE Trans. Power Deliv.* **1996**, *11*, 1379–1384. [CrossRef]
6. Mor, G.K.; Carvalho, M.A.; Varghese, O.K.; Pishko, M.V.; Grimes, C.A. A room-temperature TiO_2-nanotube hydrogen sensor able to self-clean photoactively from environmental contamination. *J. Mater. Res.* **2004**, *19*, 628–634. [CrossRef]
7. Wang, L.W.; Kang, Y.F.; Liu, X.H.; Zhang, S.M.; Huang, W.P.; Wang, S.R. ZnO nanorod gas sensor for ethanol detection. *Sens. Actuators B-Chem.* **2012**, *162*, 237–243. [CrossRef]
8. Batzill, M.; Diebold, U. The surface and materials science of tin oxide. *Progress Surf. Sci.* **2005**, *79*, 47–154. [CrossRef]
9. Myung, N.V.; Mubeen, S.; Mulchandani, A.; Deshusses, M.A. Metal and Metal Oxide Co-Functionalized Single-Walled Carbon Nanotubes for High Performance Gas Sensors. US Patent 15/090,281, 4 April 2016.
10. Cui, Y.; Wei, Q.Q.; Park, H.K.; Lieber, C.M. Nanowire nanosensors for highly sensitive and selective detection of biological and chemical species. *Science* **2001**, *293*, 1289–1292. [CrossRef] [PubMed]
11. Wang, C.X.; Yin, L.W.; Zhang, L.Y.; Xiang, D.; Gao, R. Metal oxide gas sensors: Sensitivity and influencing factors. *Sensors* **2010**, *10*, 2088–2106. [CrossRef] [PubMed]
12. Gurlo, A. Nanosensors: Towards morphological control of gas sensing activity. SnO_2, In_2O_3, ZnO and WO_3 case studies. *Nanoscale* **2011**, *3*, 154–165. [CrossRef] [PubMed]
13. Yamazoe, N. New approaches for improving semiconductor gas sensors. *Sens. Actuators B-Chem.* **1991**, *5*, 7–19. [CrossRef]
14. Schedin, F.; Geim, A.K.; Morozov, S.V.; Hill, E.W.; Blake, P.; Katsnelson, M.I.; Novoselov, K.S. Detection of individual gas molecules adsorbed on graphene. *Nat. Mater.* **2007**, *6*, 652–655. [CrossRef] [PubMed]
15. Yuan, W.J.; Shi, G.Q. Graphene-based gas sensors. *J. Mater. Chem. A* **2013**, *1*, 10078–10091. [CrossRef]
16. Zhang, D.Z.; Chang, H.Y.; Li, P.; Liu, R.H. Characterization of nickel oxide decorated-reduced graphene oxide nanocomposite and its sensing properties toward methane gas detection. *J. Mater. Sci.-Mater. Electron.* **2016**, *27*, 3723–3730. [CrossRef]

17. Abideen, Z.U.; Katoch, A.; Kim, J.H.; Kwon, Y.J.; Kim, H.W.; Kim, S.S. Excellent gas detection of zno nanofibers by loading with reduced graphene oxide nanosheets. *Sens. Actuators B-Chem.* **2015**, *221*, 1499–1507. [CrossRef]
18. Xu, S.P.; Sun, F.Q.; Pan, Z.Z.; Huang, C.W.; Yang, S.M.; Long, J.F.; Chen, Y. Reduced graphene oxide-based ordered macroporous films on a curved surface: General fabrication and application in gas sensors. *ACS Appl. Mater. Interfaces* **2016**, *8*, 3428–3437. [CrossRef] [PubMed]
19. Li, X.; Zhao, Y.; Wang, X.; Wang, J.; Gaskov, A.M.; Akbar, S. Reduced graphene oxide (rGO) decorated TiO_2 microspheres for selective room-temperature gas sensors. *Sens. Actuators B: Chem.* **2016**, *230*, 330–336. [CrossRef]
20. Latif, U.; Dickert, F.L. Graphene hybrid materials in gas sensing applications. *Sensors* **2015**, *15*, 30504–30524. [CrossRef] [PubMed]
21. Jin, L.F.; Chen, W.G.; Peng, S.Y.; Zhou, Q. Study on gas sensing properties and mechanism of Ag-doped SnO_2 gas sensor to H_2. In Proceedings of the 2015 IEEE Electrical Insulation Conference (EIC), Seattle, WA, USA, 7–10 June 2015; pp. 407–410.
22. Li, L.; Yang, H.; Zhao, H.; Yu, J.; Ma, J.; An, L.; Wang, X. Hydrothermal synthesis and gas sensing properties of single-crystalline ultralong ZnO nanowires. *Appl. Phys. A* **2010**, *98*, 635–641. [CrossRef]
23. Qi, Q.; Zhang, T.; Yu, Q.; Wang, R.; Zeng, Y.; Liu, L.; Yang, H. Properties of humidity sensing ZnO nanorods-base sensor fabricated by screen-printing. *Sens. Actuators B Chem.* **2008**, *133*, 638–643. [CrossRef]
24. Vincenzi, D.; Butturi, M.; Guidi, V.; Carotta, M.; Martinelli, G.; Guarnieri, V.; Brida, S.; Margesin, B.; Giacomozzi, F.; Zen, M. Development of a low-power thick-film gas sensor deposited by screen-printing technique onto a micromachined hotplate. *Sens. Actuators B Chem.* **2001**, *77*, 95–99. [CrossRef]
25. Ehsani, M.; Hamidon, M.N.; Toudeshki, A.; Abadi, M.S.; Rezaeian, S. CO_2 gas sensing properties of screen-printed La_2O_3/SnO_2 thick film. *IEEE Sens. J.* **2016**, *16*, 6839–6845. [CrossRef]
26. DiGiulio, M.; Micocci, G.; Serra, A.; Tepore, A.; Rella, R.; Siciliano, R. Characteristics of reactively sputtered Pt-SnO_2 thin films for CO gas sensors. *J. Vac. Sci. Technol. a-Vac. Surf. Films* **1996**, *14*, 2215–2219. [CrossRef]
27. Zhang, D.Z.; Liu, J.J.; Chang, H.Y.; Liu, A.M.; Xia, B.K. Characterization of a hybrid composite of SnO_2 nanocrystal-decorated reduced graphene oxide for ppm-level ethanol gas sensing application. *RSC Adv.* **2015**, *5*, 18666–18672. [CrossRef]
28. Dieguez, A.; Romano-Rodriguez, A.; Vila, A.; Morante, J.R. The complete Raman spectrum of nanometric SnO_2 particles. *J. Appl. Phys.* **2001**, *90*, 1550–1557. [CrossRef]
29. Zhang, H.; Feng, J.C.; Fei, T.; Liu, S.; Zhang, T. SnO_2 nanoparticles-reduced graphene oxide nanocomposites for NO_2 sensing at low operating temperature. *Sens. Actuators B-Chem.* **2014**, *190*, 472–478. [CrossRef]
30. Li, W.Q.; Ma, S.Y.; Li, Y.F.; Yang, G.J.; Mao, Y.Z.; Luo, J.; Gengzang, D.J.; Xu, X.L.; Yan, S.H. Enhanced ethanol sensing performance of hollow ZnO-SnO_2 core-shell nanofibers. *Sens. Actuators B-Chem.* **2015**, *211*, 392–402. [CrossRef]
31. Lu, G.; Ocola, L.E.; Chen, J. Reduced graphene oxide for room-temperature gas sensors. *Nanotechnology* **2009**, *20*. [CrossRef] [PubMed]
32. Chen, W.; Zhou, Q.; Gao, T.; Su, X.; Wan, F. Pd-doped SnO_2-based sensor detecting characteristic fault hydrocarbon gases in transformer oil. *J. Nanomater.* **2013**, *2013*. [CrossRef]
33. D'Amico, A.; Di Natale, C.; Sarro, P.M. Ingredients for sensors science. *Sens. Actuators B Chem.* **2015**, *207*, 1060–1068. [CrossRef]
34. Gurav, K.; Deshmukh, P.; Lokhande, C. LPG sensing properties of Pd-sensitized vertically aligned zno nanorods. *Sens. Actuators B Chem.* **2011**, *151*, 365–369. [CrossRef]
35. Uddin, A.I.; Lee, K.-W.; Chung, G.-S. Acetylene gas sensing properties of an Ag-loaded hierarchical zno nanostructure-decorated reduced graphene oxide hybrid. *Sens. Actuators B Chem.* **2015**, *216*, 33–40. [CrossRef]
36. Hosseini, Z.S.; Mortezaali, A. Room temperature H_2S gas sensor based on rather aligned ZnO nanorods with flower-like structures. *Sens. Actuators B Chem.* **2015**, *207*, 865–871. [CrossRef]
37. Kim, H.-J.; Lee, J.-H. Highly sensitive and selective gas sensors using p-type oxide semiconductors: Overview. *Sens. Actuators B Chem.* **2014**, *192*, 607–627. [CrossRef]
38. Liewhiran, C.; Tamaekong, N.; Wisitsoraat, A.; Phanichphant, S. Highly selective environmental sensors based on flame-spray-made SnO_2 nanoparticles. *Sens. Actuators B Chem.* **2012**, *163*, 51–60. [CrossRef]

39. Qi, Q.; Zhang, T.; Zheng, X.J.; Fan, H.T.; Liu, L.; Wang, R.; Zeng, Y. Electrical response of Sm_2O_3-doped SnO_2 to C_2H_2 and effect of humidity interference. *Sens. Actuators B-Chem.* **2008**, *134*, 36–42. [CrossRef]
40. Tarnaekong, N.; Liewhiran, C.; Wisitsoraat, A.; Phanichphant, S. Acetylene sensor based on Pt/ZnO thick films as prepared by flame spray pyrolysis. *Sens. Actuators B Chem.* **2011**, *152*, 155–161. [CrossRef]
41. Uddin, A.; Chung, G.S. Synthesis of highly dispersed ZnO nanoparticles on graphene surface and their acetylene sensing properties. *Sens. Actuators B-Chem.* **2014**, *205*, 338–344. [CrossRef]
42. Hotovy, I.; Huran, J.; Siciliano, P.; Capone, S.; Spiess, L.; Rehacek, V. Enhancement of H_2 sensing properties of nio-based thin films with a pt surface modification. *Sens. Actuators B Chem.* **2004**, *103*, 300–311. [CrossRef]
43. Singkammo, S.; Wisitsoraat, A.; Sriprachuabwong, C.; Tuantranont, A.; Phanichphant, S.; Liewhiran, C. Electrolytically exfoliated graphene-loaded flame-made ni-doped SnO_2 composite film for acetone sensing. *ACS Appl. Mater. Interfaces* **2015**, *7*, 3077–3092. [CrossRef] [PubMed]
44. Russo, P.A.; Donato, N.; Leonardi, S.G.; Baek, S.; Conte, D.E.; Neri, G.; Pinna, N. Room-temperature hydrogen sensing with heteronanostructures based on reduced graphene oxide and tin oxide. *Angew. Chemie Int. Ed.* **2012**, *51*, 11053–11057. [CrossRef] [PubMed]
45. Lin, Q.Q.; Li, Y.; Yang, M.J. Tin oxide/graphene composite fabricated via a hydrothermal method for gas sensors working at room temperature. *Sens. Actuators B-Chem.* **2012**, *173*, 139–147. [CrossRef]